Geochemical Perspectives Letters

^{182}W evidence for core-mantle interaction in the source of mantle plumes

H. Rizo, D. Andrault, N.R. Bennett, M. Humayun, A. Brandon, I. Vlastelic, B. Moine, A. Poirier, M.A. Bouhifd, D.T. Murphy

Supplementary Information

The Supplementary Information includes:

- 1. Sample Description
- 2. Analytical Methods for W Concentrations and Isotope Measurements
- 3. Correlations Between ^{182}W and ^{3}He/^{4}He and Fe/Mn Ratios
- 4. Evidence for W Solubility in Exsolved Oxides and Decoupling of W and HSE Abundances
- Tables S-1 to S-4
- Figures S-1 to S-6
- Supplementary Information References

1. Sample Description

1.1. Réunion Island Samples

Réunion Island samples are fresh lavas produced during the recent (1986-2010) activity of the Piton de la Fournaise volcano. Sample REU 863-204 is from the March 1986 eruption, which propagated along the South-East rift zone. This rock sample was collected at Ravine Takamaka (880 m elevation). Sample REU 0609-131 was collected during the August 2006 summit eruption, which occurred entirely within the Dolomieu crater at 2500 m. The molten lava was quenched in water immediately after sampling. Samples REU 1001-053 and REU 1406-24.9a are lapilli emitted on the upper flanks of the Dolomieu Crater during the January 2010 and June 2014 eruptions, respectively. Sample REU 863-204 is poorly phyric, whereas the other three samples are mostly glassy. A detailed description of the composition of the samples is provided in Vlastélic *et al.* (2009; 2013; 2018) and Gurioli *et al.* (2017) and only the main characteristics are given here. Major element compositions are transitional between alkali basalts and tholeiites, as are most Réunion Island shield lavas. The samples have 6.5-8.0 wt. % MgO, 67-134 ppm Ni, and 54-270 ppm Cr, and belong to a dominant, homogeneous lava group often named "Steady State Basalts". The ^{87}Sr/^{86}Sr (0.704136-0.704200) and ^{206}Pb/^{204}Pb (18.901-18.930) ratios of the samples plot in the middle of the narrow isotope field of Réunion Island samples.

1.2. Kerguelen Archipelago Samples

Since the Cretaceous Kerguelen Plateau basalts are known to have assimilated shallow-level continental crust materials (*e.g.*, Ingle *et al.*, 2003), all the samples studied here were collected from the Kerguelen Archipelago, which is the Cenozoic part of the Plateau. Some of these more recent lavas might reflect some degree of mixing with depleted upper mantle or assimilated overlying

Cretaceous lithosphere, but given the low expected W concentration of these contaminants, the Kerguelen Archipelago samples remain the best candidates for this study. Samples were collected during field seasons of summer 2002 (CarbonatoKer program) and 2006 (DyLIOKer program of the Institut Polaire Français). All of the samples studied here are high-MgO basalts containing olivine and clinopyroxene phenocrysts. These rock types represent the less differentiated liquids, with little to no crustal contamination, and are the most representative of the mantle plume signature (minimum mixing with Indian mid ocean ridge basalts and/or lithospheric components).

Kerguelen sample CT02-358 comes from Monts Aubert de la Rue (S49°36′42″ E69°40′50″), with estimated emplacement age between 18-20 Ma. Sample CT02-548 is a phonolite collected in Val Phonolite (south west of Presqu'ile Ronarc'h, S49°35′52″ E70°05′25″) with eruption dates between 6-12 Ma. Sample TC06-03 is from the Peninsula of Loranchet (Port Léontine S48°58′54″ E69°59′21″), with an estimated emplacement age between 19-24 Ma. Similar samples (CT02-373, CT02-376 and RR08-123) from the same locations were analysed for He isotope compositions and yielded R/Ra ratios between 10.6 and 12.46 (Doucet *et al.*, 2005; 2006).

The three Kerguelen samples were measured here for Pb isotopes at the Geotop laboratoires (Université du Québec à Montréal) and results are given in Table S-1. Measurements were performed on a Nu Plasma II using the Aridus II desolvating membrane as the introduction device. Lead isotope compositions were corrected for mass bias using Tl addition and measuring Pb standard NBS981 as in Woodhead (2002). Reproducibility over 6 years of measurement of our in-house secondary standard solution CGPB-1 shows 2-sigma uncertainties of 204-normalised ratios in the 3rd decimal place, and 4th decimal place for the 206-normalised ones. Full procedural blank yielded 16 pg of common Pb. In Pb-Pb isotopic space, the values obtained here fall onto the array defined by Doucet *et al*. (2005), between NMORB and the Kerguelen plume components.

1.3. Pilbara Craton Samples

Pilbara Craton samples are lower greenschist facies meta-basalts retrieved from coherent outcrops of pillow lavas in the Doolena Gap greenstone belt of the East Pilbara Terrane. The samples are from the 3.475 Ga Mt Ada Basalts of the Warrawoona Group (Kranendonk *et al.*, 2002). Both samples were retrieved from the low strain belt of the western Doolena Gap greenstone belt as defined by Wiemer *et al.* (2016) (AH25; S20°54′20″ E119°43′1″, AH26; S20°54′15″ E119°43′7″). The two outcrops represent lozenges of well-preserved overturned pillow lavas that are surrounded by altered and deformed mafic schists. A detailed description of the stratigraphy and structure of the western Doolena Gap greenstone belt is provided in Wiemer *et al.* (2016).

The samples have a preserved microcrystalline texture defined by altered plagioclase laths. Rare microphenocrysts of plagioclase are present with poorly preserved polysynthetic twinning. Clinopyroxene is rarely present as microcrysts. Equant carbonate features with spinel inclusions are interpreted as pseudomorphs after olivine. Fine-grained epidote, chlorite and carbonate are pervasive throughout the samples.

The two Pilbara Craton samples were measured for major element and trace element chemistry at the Central Analytical Research Facility (CARF), Queensland University of Technology. The results are reported in Table S-2. Major elements were analysed using a WDS XRF Pananalytical Axois 1 kW system. Powdered samples were ignited for *ca*. 3 hours in ceramic crucibles at 950 °C to measure loss on ignition. Trace element analyses were performed with an Agilent 8800 triple quadrupole ICP-MS. 50 mg of sample were dissolved in a mixture of 1.5 mL double distilled HCl, 0.5 mL double distilled HNO_3 and 0.5 mL double distilled HF in PTFE vials using a Milestone bench-top Ultra-wave microwave digestion system. The samples were then transferred to a hotplate at 80-100 °C to evaporate HF in repeated steps of adding HNO_3 and MilliQ, and then washed and centrifuged. Internal standards 9Be, 103Rh, 115In and 209Bi were added to aliquots of the solution for internal standard correction. The geological reference materials W-2 and AGV-2 were analysed as standards.

2. Analytical Methods for W Concentrations and Isotope Measurements

Samples were crushed with metal-free tools to avoid any metal contamination (plastic hammers, ceramic or agate jaw crushers and mortars). All W concentrations (Table S-3) were determined by isotope dilution using a ^{186}W tracer and ~200 mg of rock powder material. Samples were spiked and digested using concentrated HF-HNO_3, followed by repeated dry downs and re-dissolutions in 6N HCl. Once samples were dissolved, W was separated from bulk samples using an anion exchange column with 1ml of AG1-X8 (100-200 mesh) resin. Tungsten concentrations were acquired either using the MC-ICP-MS Nu Plasma II at Geotop laboratories in Montréal or the ICP-MS Triple Quad at the Department of Earth and Environmental Sciences of the University of Ottawa. Total chemistry blanks were typically < 0.2 ng W, representing ~0.3 % of the W measured.

For high-precision W isotope analyses, sample powders were dissolved in order to extract 500-1000 ng of W. Samples were dissolved in concentrated HF-HNO_3 in closed beakers for 4-5 days. Then the samples were dried down and re-dissolved several times in concentrated HNO_3 and then in 6N HCl. Tungsten was then separated from the bulk rock using a similar protocol to the one detailed in Breton and Quitté (2014) and only brief details are given here. Before column chemistry, dissolving the sample in

HF 1N and extracting the supernatant after centrifuging it removes Ca-Mg fluorides, which can incorporate some W. Tungsten was then separated using an anion column filled with 10 mL AG1-X8 (200-400 mesh) resin, and further purified using a column filled with ~ 300 µL of the same AG1-X8 resin. Tungsten recovery using this method was between 80 % and 95 %.

Tungsten isotope compositions were measured on Re filaments as trioxide species (WO_3^-) in the Thermo-Fisher Triton thermal ionisation mass spectrometer (TIMS) at the Department of Earth Sciences of Carleton University in Ottawa. Tungsten oxides were ionised using a mixed solution of La and Gd that acted as an electron emitter and bleeding O_2 into the source, with a source pressure fixed at $1.15e^{-7}$ mbar that facilitates W oxide production. Tungsten isotopes were measured using a similar analytical protocol to the one described in Archer *et al.* (2017), where major oxide species (*e.g.*, $W^{16}O_3$) are measured in Faraday cups electronically connected to 10^{11} ohm resistors, and the low signals $^{186}W^{16}O_2{}^{18}O^-$ and $^{187}Re^{16}O_2{}^{18}O^-$ are measured in Faraday cups connected to 10^{12} ohm resistors. These low signals were used to calculate per-integration oxide corrections to derive the different W isotope ratios. The analyses performed here use a multistatic method consisting of three steps of acquisition with $^{184}W.O_3$, $^{185}Re.O_3$ and $^{187}Re.O_3$ masses placed in the central cup, respectively. Step 1 measures the low signals $^{186}W^{16}O_2{}^{18}O^-$ and $^{187}Re^{16}O_2{}^{18}O^-$ and thus the integration time for this step is 33 s and 12 s for the idle time. Step 2 and step 3 use an 8s integration time and 4 s idle time. Baselines were measured for 1200 s every 7 blocks, and peak centre and lens focus were performed every 3 blocks. Step 1 and 2 are averaged to obtain mean $^{182}W/^{184}W$ and $^{183}W/^{184}W$ ratios. One tungsten isotope measurement represents the average of 560 cycles, measured in 28 blocks of 20 cycles. All tungsten isotope ratios shown in Table S-4 have been corrected for instrumental fractionation using the $^{186}W/^{184}W$ ratio of 0.927670 (Völkening *et al.*, 1991).

Potential analytical problems with the measurement of ^{183}W have been recently reported (Cook and Schönbachler, 2016; Kruijer and Kleine, 2018), where deviations in the stable ^{183}W were measured. These deviations have been attributed to preferential loss of W of the odd mass isotope ^{183}W during the chemical extraction of W from a rock matrix. They suggested that this ^{183}W loss was possibly a result of a nuclear field shift effect that could also affect ^{182}W. None of the samples or standards measured here show resolvable ^{183}W deviations from the isotopic composition of the W terrestrial standard (Figs. S-1 and S-2).

3. Correlations between ^{182}W and $^{3}He/^{4}He$ and Fe/Mn Ratios

Recent high-precision W isotope measurements of rock samples from Hawaii, Samoa and Iceland reported resolvable deficits in ^{182}W compared to terrestrial standard that correlate with $^{3}He/^{4}He$ ratios (Mundl *et al.*, 2017). Furthermore, the Earth's core has been proposed as an important reservoir of He (*e.g.*, Bouhifd *et al.*, 2013; Trieloff and Kunz, 2005), making core-mantle interaction a possible explanation for the ^{182}W *vs.* $^{3}He/^{4}He$ correlation. These ^{182}W observations, however, were difficult to explain by this process since W and Os isotopic compositions were not correlated and the source of these rocks lacked any apparent increase in the abundances of HSE. Estimating HSE source abundances of partial melts is, however, challenging since these elements are affected by several processes including partial melt and fractional crystallisation, as well as sulphide precipitation and mantle oxygen fugacity. Therefore, despite the lack of ^{182}W *vs.* HSE correlation, ^{182}W *vs.* $^{3}He/^{4}He$ characteristics could still translate core-mantle interaction processes.

Core-mantle chemical interaction may also affect Fe abundances in the sources of plumes. This could be detected by precisely measuring the Fe/Mn ratio of plume-related magmas, since Mn is more lithophile than Fe. During partial melting and fractional crystallisation of mantle melts, the Fe/Mn ratio is perturbed less than the FeO abundance. Higher Fe/Mn (10-20 %) in the sources of mantle plumes, particularly Hawaiian lavas, relative to MORB has been documented for several plumes (Humayun *et al.*, 2004; Qin and Humayun, 2008; Vlastélic *et al.*, 2006). During deep (>100 km) partial melting of mantle plumes, pyroxenite residues could also increase the silica contents and Fe/Mn ratios, the latter by preferential retention of Mn in garnet-cpx-rich sources (Sobolev *et al.*, 2007). The constant Fe/Mn ratios from Loihi to Koolau Hawaiian lavas, together with variable Si contents, could argue against pyroxenite residues playing an important role in Fe/Mn variations in Hawaii (Huang *et al.*, 2007).

For each of the locations for which $\mu^{182}W$ data were available, and for the locations for which new $\mu^{182}W$ results are reported here, the available values of Fe/Mn were compiled (Fig. S-4). While FeO and MnO are reported in every major element analysis, two considerations greatly limit the availability of precise Fe/Mn data: (i) rounding error is significant when MnO is reported to only two decimal places, and (ii) alteration affects the Fe/Mn ratio for all but fresh lavas or mineral compositions. Fresh lavas are routinely collected from historic eruptions at Piton de la Fournaise, Reunion, and precise MnO values are available for these lavas (Vlastélic *et al.*, 2006). The mean Fe/Mn value obtained from glasses studied by Vlastélic *et al.* (2006) are identical to the single analysis from Qin and Humayun (2008). Data for Hawaii (Humayun *et al.*, 2004), Iceland and MORB (Qin and Humayun 2008), and the Azores (Humayun, *unpublished*) were based on average values for each of the localities. For the Azores, Fe/Mn data from basalts from Pico Island were taken to match as closely as possible the samples for which $\mu^{182}W$ were available.

4. Evidence for W solubility in Exsolved Oxides and Decoupling of W and HSE Abundances

For Si-Mg-Fe oxides to act as a vehicle for core-mantle exchange of tungsten, they must be able to dissolve this element in appreciable amounts. Furthermore, they must provide a means for fractionating W from the HSEs. There is a paucity of published experiments designed specifically to determine W and HSE partitioning between metallic and oxide melts. However, there is evidence in the literature, and from our own experiments, that FeO-rich oxide melts will both concentrate W and exclude the HSEs relative to Fe-rich metallic melts.

First, we will consider evidence for the solubility of W in exsolved oxides. Figure S-5 displays the run product from a laser-heated diamond anvil cell (LH-DAC) experiment performed at ~24 GPa (cold pressure determined by ruby fluorescence) and 3250 K; conditions where significant amounts of oxygen can dissolve into Fe-rich metallic melt. This experiment was performed with the goal of determining the metal-silicate partitioning of W at high temperature and pressure, but also provides useful information for the present discussion. The starting material was approximately chondritic in composition (C1/C from Thibault and Walter, 1995) that was doped with ~8 wt. % tungsten metal. The sample was heated at beamline 13-ID-D at the Advanced Photon Source using a flat-top fibre laser and quenched by cutting power to the laser. The quenched metallic melt forms a roughly spherical bead at the centre of the heated region, which is mantled by a layer of silicate melt. When the sample is quenched, the decrease in temperature causes saturation of the metallic melt in an FeO-rich oxide phase – now seen as the exsolved darker-grey blebs within the main metal phase. Similar textures were also observed in the W metal-silicate partitioning experiments performed by Shofner *et al.* (2011; 2016). Figure S-5 displays WDS maps for O, Si, Ni, and W for the quenched sample that were acquired with a JEOL 8530F field-emission microprobe located at the Carnegie Institution of Washington, using a 10 kV accelerating voltage and 10 nA beam current. These maps show that W, O, and Si are preferentially concentrated in the exsolved oxide phase relative to the metal, whereas Ni remains concentrated in the metallic melt. These quench textures demonstrate that significant solubility of W in oxide melt is possible, and provide a crude but encouraging hint that W may preferentially partition into this phase over the metallic melt. It is noteworthy that Ni retains its siderophile nature in the presence of an oxide melt, whereas W does not, as some previous partitioning experiments appear to predict these behaviours. Chabot *et al.*, (2015) investigated trace element partitioning between coexisting melts in the Fe-S-O system, in which one melt contains high O concentrations (6–14 wt. %) and the other is essentially O-free. They found that most siderophile elements, including Ni, display O-avoiding behaviour; partitioning more strongly into the O-free melt with increasing O concentrations in the O-rich melt. Tungsten, however, displays the opposite behaviour and partitions more strongly into the O-rich phase as its O content increases. The fact that these trends are reflected in the element distribution of quenched LH-DAC experiments provides encouragement that the qualitative sense of W partitioning between metal and oxide melt is being captured. Furthermore, Shofner *et al.*, (2016) determined the thermal equation of state (EOS) for W and WO_2 and, using the EOS for IW determined by Campbell *et al.*, (2009), demonstrated that for a given T and fO_2, increasing pressure favours the formation of WO_2. At the pressures of the outer core, partitioning of W into exsolved oxide may therefore be enhanced relative to that suggested by our LH-DAC experiment done at only ~24 GPa.

We can also use the results of the Chabot *et al.*, (2015) experiments to assess the likelihood of the HSE being fractionated from W by exsolution of an oxide phase from the core. Unlike W, which displays a preference for oxygen in those experiments, the HSEs universally display O-avoidance behaviour. If, as for Ni and W, the Chabot *et al.*, (2015) experiments provide a pointer to the sense of partitioning between metal and oxide melts, we should expect HSEs to remain concentrated in the metallic melt upon exsolution of an oxide phase. We can again turn to experimental quench textures for support of this prediction.

Fortenfant *et al.* (2003) equilibrated metallic liquids with magnesiowüstite, to investigate the partitioning of Re, Os, and Ni. These experiments were performed at 5 – 10 GPa and 2173 – 2473 K using a multi-anvil apparatus. The authors observed that the quenched metal in these experiments often contained ~2-20 μm blebs of oxygen-bearing liquid iron. The volumetric proportion of these blebs in the metal phase is low, and including them in the analysis of the bulk metal phase had a negligible result on the measured Re and Os concentrations. The authors therefore conclude that the concentrations of Re and Os in the blebs are low (Fortenfant *et al.*, 2003). The metal-magnesiowüstite partition coefficients reported by Fortenfant *et al.*, (2003) may also provide some indication of how HSEs partition between metallic and oxide liquids. The authors find that all three elements they investigated are incompatible in magnesiowustite relative to metal, with incompatibility increasing in the order Ni < Re < Os. This suggests Re and Os will be concentrated in the metal phase during exsolution of an oxide melt. We also note that the incompatibility of Ni in magnesiowustite found by Fortenfant *et al.*, (2003) is in qualitative agreement with our LH-DAC experiment, which shows Ni prefers to remain in the metallic phase.

Bennett *et al.* (2014) presented preliminary results of Soret experiments in the Fe-Ni-O system that were doped with W, Mn, and the HSEs. Samples comprised powdered starting materials encapsulated in alumina and positioned below the hot-spot of a 14/8 multi-anvil assembly, in order to maximise the thermal gradient across the sample. During the experiment, major element gradients develop as a result of heat of transport effects. Trace elements are then redistributed in response to the major element gradient according to their activity-composition relationships. This leads to the alloy at the hot end of the sample being enriched in oxygen. When the sample is quenched, this O-enriched liquid alloy becomes saturated in O and liquid FeO-rich blebs are exsolved. As with the LH-DAC sample in Figure S-5, the composition of these exsolved blebs can provide qualitative clues about the sense of metallic liquid-oxide liquid trace element partitioning. Figure S-6 displays time-resolved LA-ICPMS spectra for one of these

samples, from an experiment performed at 15 GPa and with a temperature at the hot-spot of the assembly of ~2600 K. During analysis, the laser was rastered across the sample surface, to include regions both with and without FeO blebs. Regions of oxide ablation are easily identified in the time-resolved spectra by higher than average counts per second of W and Mn and lower than average counts per second of the HSEs (Figs. S-6a and S-6b respectively). Analyses of the alloy away from the hot end of the sample, where FeO blebs are not observed, show homogeneous time-resolved profiles for all elements. These results qualitatively follow the behaviours observed by Chabot *et al*., (2015) in the Fe-S-O system and support the idea that W is fractionated from the HSEs by metallic liquid-oxide liquid partitioning.

Experiments designed specifically to determine metallic liquid-oxide liquid partitioning for W and the HSEs are clearly needed to rigorously test the suitability of oxide melts for fractionating W from the HSEs. However, we believe that the above observations are a useful starting point for future study and provide evidence that oxides exsolved from the core are a plausible agent for transporting W from the core to the mantle.

Supplementary Tables

Table S-1 Pb isotope compositions for Kerguelen Archipelago samples.

Sample	$^{208}Pb/^{204}Pb$	$^{207}Pb/^{204}Pb$	$^{206}Pb/^{204}Pb$	$^{207}Pb/^{206}Pb$	$^{208}Pb/^{206}Pb$
TC0603	38.805	15.547	18.319	0.8487	2.1184
CT02358	39.175	15.559	18.563	0.8382	2.1105
CT02548	39.021	15.569	18.432	0.8447	2.1171

Table S-2 Major and trace element concentrations for Pilbara samples.

Concentration (wt. %)	AH25	AH26	Concentration (ppm)	AH25	AH26	Concentration (ppm)	AH25	AH26
SiO_2	48.76	47.68	Li	15.24	15.02	U	0.06	0.19
TiO_2	0.91	1.53	Sc	42.54	36.54	Ba	34.59	34.11
Al_2O_3	15.44	13.16	Ti	5575	9981	La	1.97	7.82
Fe_2O_3	10.25	17.12	V	266.7	312.7	Ce	5.89	20.04
MnO	0.17	0.25	Cr	329.2	119.6	Pr	0.97	3.00
MgO	4.24	6.07	Co	52.65	54.07	Nd	5.06	14.42
CaO	6.59	7.89	Ni	153.5	78.46	Sm	1.73	4.08
Na_2O	6.12	1.98	Cu	119.5	119.6	Eu	0.55	1.12
K_2O	0.71	0.41	Zn	90.45	131.3	Gd	2.18	4.54
P_2O_5	0.07	0.13	Rb	9.29	6.17	Tb	0.42	0.81
LOI	7.02	5.70	Sr	56.13	268.3	Dy	2.87	5.24
Total	100.46	102.32	Y	15.18	31.90	Ho	0.62	1.12
			Zr	55.95	111.0	Er	1.80	3.20
			Nb	2.16	6.14	Tm	0.27	0.50
			Mo	0.00	0.14	Yb	1.82	3.17
			Cd	0.00	0.00	Lu	0.27	0.50
			Sb	0.00	0.01	Hf	1.49	2.94
			Cs	0.12	0.11	Ta	0.14	0.35
			Pb	0.64	1.45	Ba	34.59	34.11
			Th	0.22	0.82			

Table S-3 Tungsten concentrations of all samples studied.

Location	Sample	Lithology	W (ppb)
Hawaii	BHVO-2	Basalt	224
Réunion Island	REU 1406-24.9a	Basalt	320
Réunion Island	REU 1001-053	Basalt	317
Réunion Island	REU 863-204	Basalt	364
Réunion Island	REU 0609-131	Basalt	309
Kerguelen Archipelago	TC0603b	Alkaline basalt	589
Kerguelen Archipelago	CT02-358	Alkaline basalt	387
Kerguelen Archipelago	CT02-548	Alkaline basalt	299
Pilbara	AH25	Pillow metabasalt	59
Pilbara	AH26	Pillow metabasalt	96

Table S-4 Detailed W isotope data for the Réunion Island, the Kerguelen Archipelago and the Pilbara Craton samples

Location	Sample	Analytical session	$^{185}Re/^{184}W$	$^{181}Ta/^{184}W$	*Static line 1*		*Static line 2*		*Mean line 1 + line 2*		$\mu^{182}W$	$\mu^{183}W$
					$^{182}W/^{184}W$	$^{183}W/^{184}W$	$^{182}W/^{184}W$	$^{183}W/^{184}W$	$^{182}W/^{184}W$	$^{183}W/^{184}W$		
Réunion Island	REU 1001-053	1	0.28	2.3E-06	0.864870 ± 3	0.467111 ± 1	0.864882 ± 6	0.467116 ± 3	0.864877 ± 3	0.467114 ± 2	-19.0 ± 4.0	-3.3 ± 3.5
	REU 1001-053 duplicate	1	0.26	8.7E-07	0.864870 ± 4	0.467112 ± 2	0.864894 ± 8	0.467119 ± 3	0.864882 ± 4	0.467114 ± 2	-12.4 ± 5.0	-1.6 ± 4.0
	REU 1406-24.9a	1	0.14	8.3E-07	0.864865 ± 5	0.467108 ± 2	0.864887 ± 8	0.467118 ± 4	0.864876 ± 4	0.467113 ± 2	-20.2 ± 5.1	-5.8 ± 4.7
	REU 863-204	2	0.02	-3.7E-06	0.864892 ± 4	0.467119 ± 2	0.864895 ± 5	0.467116 ± 2	0.864893 ± 3	0.467117 ± 2	-8.7 ± 3.8	0.7 ± 3.3
	REU 863-204 duplicate	1	0.14	1.1E-07	0.864881 ± 3	0.467113 ± 1	0.864891 ± 6	0.467118 ± 3	0.864885 ± 3	0.467115 ± 2	-9.2 ± 4.0	-0.8 ± 3.4
	REU 0609-131	2	0.02	-3.7E-06	0.864889 ± 6	0.467118 ± 3	0.864903 ± 6	0.467116 ± 3	0.864894 ± 5	0.467117 ± 2	-7.6 ± 5.3	0.4 ± 4.7
	REU 0609-131 duplicate	1	0.04	3.7E-06	0.864882 ± 3	0.467115 ± 1	0.864891 ± 6	0.467118 ± 3	0.864885 ± 3	0.467117 ± 1	-8.8 ± 3.9	4.0 ± 3.2
Kerguelen Archipelago	TC0603	1	0.07	1.6E-06	0.864875 ± 7	0.467111 ± 3	0.864879 ± 12	0.467116 ± 5	0.864879 ± 7	0.467114 ± 3	-16.5 ± 8.5	-3.1 ± 5.8
	TC0603 duplicate	1	0.04	1.4E-06	0.864880 ± 3	0.467113 ± 2	0.864890 ± 6	0.467120 ± 3	0.864887 ± 3	0.467116 ± 2	-7.3 ± 4.0	2.1 ± 3.4
	CT02-358	1	0.04	1.7E-06	0.864876 ± 6	0.467111 ± 3	0.864895 ± 12	0.467119 ± 6	0.864885 ± 6	0.467114 ± 3	-9.4 ± 7.4	-2.8 ± 7.2
	CT02-358 duplicate	1	0.02	1.0E-06	0.864881 ± 3	0.467113 ± 1	0.864894 ± 4	0.467119 ± 2	0.864887 ± 3	0.467116 ± 1	-7.4 ± 3.0	1.9 ± 2.6
	CT02-548	1	0.03	1.5E-06	0.864878 ± 4	0.467114 ± 2	0.864882 ± 7	0.467118 ± 3	0.864880 ± 4	0.467116 ± 2	-15.2 ± 4.6	1.1 ± 3.7
Pilbara Craton	AH-25	1	0.03	3.2E-07	0.864892 ± 3	0.467113 ± 1	0.864917 ± 6	0.467123 ± 3	0.864904 ± 4	0.467118 ± 2	13.1 ± 4.1	5.2 ± 3.5
	AH-26	1	0.07	4.4E-07	0.864902 ± 4	0.467116 ± 2	0.864911 ± 7	0.467117 ± 3	0.864906 ± 4	0.467116 ± 2	15.3 ± 4.6	2.4 ± 3.7
	Alfa Aesar W standards	1	0.01	1.5E-06	0.864890 ± 3	0.467115 ± 1	0.864891 ± 6	0.467116 ± 3	0.864892 ± 3	0.467117 ± 1	-1.3 ± 3.5	2.9 ± 3.2
			0.01	5.8E-07	0.864892 ± 3	0.467114 ± 2	0.864899 ± 6	0.467118 ± 3	0.864895 ± 4	0.467116 ± 2	2.6 ± 4.3	1.4 ± 3.7
			0.01	9.1E-07	0.864888 ± 4	0.467114 ± 2	0.864901 ± 7	0.467116 ± 3	0.864893 ± 4	0.467115 ± 2	0.0 ± 4.3	0.0 ± 3.9
			0.01	1.2E-06	0.864892 ± 4	0.467115 ± 2	0.864901 ± 7	0.467120 ± 3	0.864895 ± 4	0.467117 ± 2	1.8 ± 4.9	4.5 ± 4.3
			0.01	5.4E-07	0.864885 ± 5	0.467111 ± 2	0.864897 ± 9	0.467117 ± 4	0.864892 ± 5	0.467114 ± 2	-1.6 ± 5.9	-2.5 ± 5.3
			0.02	1.2E-06	0.864880 ± 4	0.467111 ± 2	0.864898 ± 8	0.467122 ± 4	0.864890 ± 4	0.467114 ± 2	-3.9 ± 5.1	-2.6 ± 4.4
			0.03	1.1E-07	0.864886 ± 5	0.467113 ± 2	0.864892 ± 10	0.467118 ± 5	0.864892 ± 5	0.467116 ± 2	-1.5 ± 6.0	2.2 ± 5.0
			0.02	8.9E-07	0.864882 ± 5	0.467108 ± 2	0.864900 ± 10	0.467119 ± 4	0.864890 ± 6	0.467114 ± 3	-3.5 ± 6.6	-2.5 ± 5.4
			0.02	2.5E-07	0.864887 ± 4	0.467110 ± 2	0.864906 ± 8	0.467116 ± 4	0.864894 ± 5	0.467114 ± 2	1.4 ± 5.4	-3.6 ± 4.4
			0.02	1.8E-06	0.864885 ± 4	0.467111 ± 2	0.864900 ± 7	0.467121 ± 4	0.864894 ± 4	0.467116 ± 2	1.4 ± 4.8	2.2 ± 4.3
			0.01	6.0E-07	0.864893 ± 4	0.467113 ± 2	0.864900 ± 7	0.467116 ± 3	0.864896 ± 4	0.467114 ± 2	3.6 ± 4.6	-1.8 ± 3.9
			0.02	9.8E-07	0.864885 ± 4	0.467112 ± 2	0.864900 ± 7	0.467117 ± 3	0.864894 ± 4	0.467115 ± 2	1.0 ± 4.6	0.0 ± 4.0

Table S-4 ***(continued)*** Detailed W isotope data for the Réunion Island, the Kerguelen Archipelago and the Pilbara Craton samples.

Location	Sample	Analytical session	$^{185}Re/^{184}W$	$^{181}Ta/^{184}W$	*Static line 1*		*Static line 2*		*Mean line 1 + line 2*		$\mu^{182}W$	$\mu^{183}W$
					$^{182}W/^{184}W$	$^{183}W/^{184}W$	$^{182}W/^{184}W$	$^{183}W/^{184}W$	$^{182}W/^{184}W$	$^{183}W/^{184}W$		
	Alfa Aesar W standards	2	0.02	-5.2E-06	0.864893 ± 7	0.467114 ± 3	0.864906 ± 6	0.467115 ± 3	0.864900 ± 5	0.467115 ± 2	-0.9 ± 5.3	-5.5 ± 4.6
			0.04	-4.0E-06	0.864904 ± 7	0.467123 ± 3	0.864899 ± 7	0.467115 ± 3	0.864903 ± 5	0.467118 ± 2	2.4 ± 5.8	2.8 ± 4.6
			0.10	-2.8E-06	0.864906 ± 6	0.467117 ± 3	0.864903 ± 6	0.467119 ± 3	0.864905 ± 4	0.467118 ± 2	5.0 ± 5.0	2.2 ± 4.5
			0.05	-2.5E-06	0.864898 ± 6	0.467115 ± 3	0.864902 ± 6	0.467117 ± 3	0.864902 ± 4	0.467116 ± 2	1.6 ± 4.8	-2.2 ± 4.2
			0.07	-3.7E-06	0.864898 ± 4	0.467121 ± 2	0.864903 ± 5	0.467114 ± 2	0.864899 ± 3	0.467117 ± 2	-2.0 ± 3.6	-0.5 ± 3.3
			0.04	-4.1E-06	0.864896 ± 4	0.467118 ± 2	0.864904 ± 4	0.467115 ± 2	0.864899 ± 3	0.467117 ± 1	-2.6 ± 3.0	-0.4 ± 2.8
			0.03	-1.9E-06	0.864893 ± 7	0.467118 ± 3	0.864904 ± 7	0.467120 ± 3	0.864898 ± 4	0.467119 ± 2	-3.5 ± 5.2	3.6 ± 4.4

Notes: Precision for isotope ratios is given is ± 2 s.e. on last decimals place. Tungsten isotope ratios are also reported in μ values ± 2 s.e. (ppm) relative to the W standard measured during the same analytical session as the samples.

Supplementary Figures

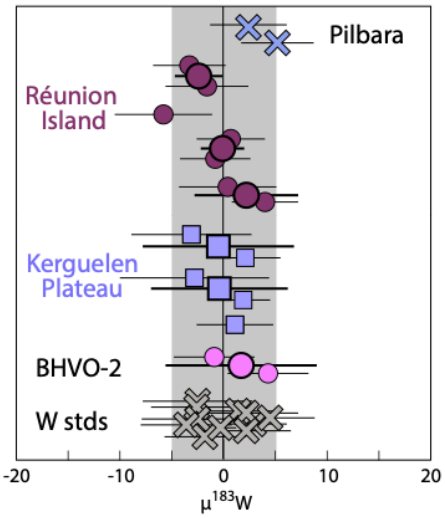

Figure S-1 $^{183}W/^{184}W$ data obtained in this study, shown as $\mu^{183}W$ values, which are relative deviations of the W isotope composition of the samples from the terrestrial standard in parts per million (ppm) ($\mu^{183}W = [(^{183}W/^{184}W)_{sample}/(^{183}W/^{184}W)_{standard}]-1)*10^6$). Small symbols are individual analysis of samples with errors in 2 s.e.; larger symbols show the average of the different duplicates, with respective 2 s.d. errors. The shaded area represents the reproducibility obtained (2 s.d.) on repeated measurements of the Alfa Aesar W standard.

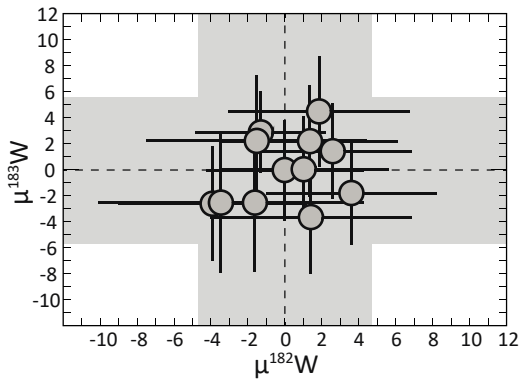

Figure S-2 $\mu^{182}W$ *vs.* $\mu^{183}W$ values for tungsten standard measurements performed in this study. The shaded area represents the reproducibility obtained (2 s.d.) on repeated measurements of the Alfa Aesar W standard.

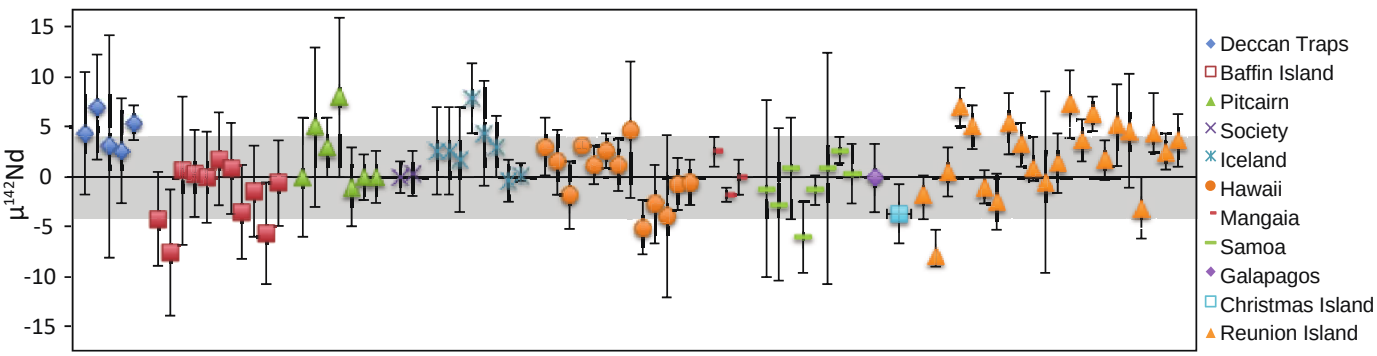

Figure S-3 $^{142}Nd/^{144}Nd$ data of plume-related rock samples. $^{142}Nd/^{144}Nd$ is shown as $\mu^{142}Nd$ values, which is the deviation in ppm from the Nd terrestrial standard ($\mu^{142}Nd$ = 0). The shaded area represents the typical reproducibility obtained (2 s.d.) obtained on repeated measurements of the Nd terrestrial standard. Data from Andreasen *et al.* (2008), Boyet and Carlson (2006), Caro *et al.,* (2006), de Leeuw *et al.* (2017), Garçon *et al.* (2018), Horan *et al.* (2018), Jackson *et al.* (2012), Murphy *et al.* (2010), and Peters *et al.* (2018).

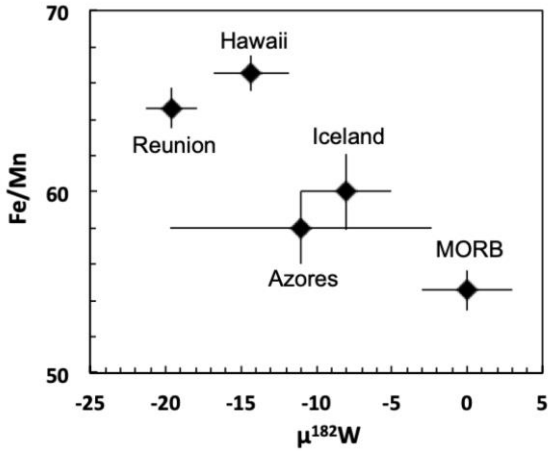

Figure S-4 Comparison of the potential core-mantle interaction tracer Fe/Mn in OIB suites that have been analysed for $\mu^{182}W$. Only averages of the lowest $\mu^{182}W$ for each of the OIB localities are shown (see Fig. 2 of the main manuscript for sources). Average of Fe/Mn ratios reported for MORB, Iceland, Pico (Azores), Reunion, and Hawaii (Humayun *et al.*, 2004; Qin and Humayun, 2008; Vlastélic *et al,* 2006; Humayun, *unpublished*). For Azorean samples shown, $\mu^{182}W$ and Fe/Mn are both limited to Pico Island lavas, which do not represent the same samples but represent the same lava flows for most samples. For Hawaii, all three tracers were measured on at least some of the same samples, while for Iceland Fe/Mn ratios were measured on the same samples.

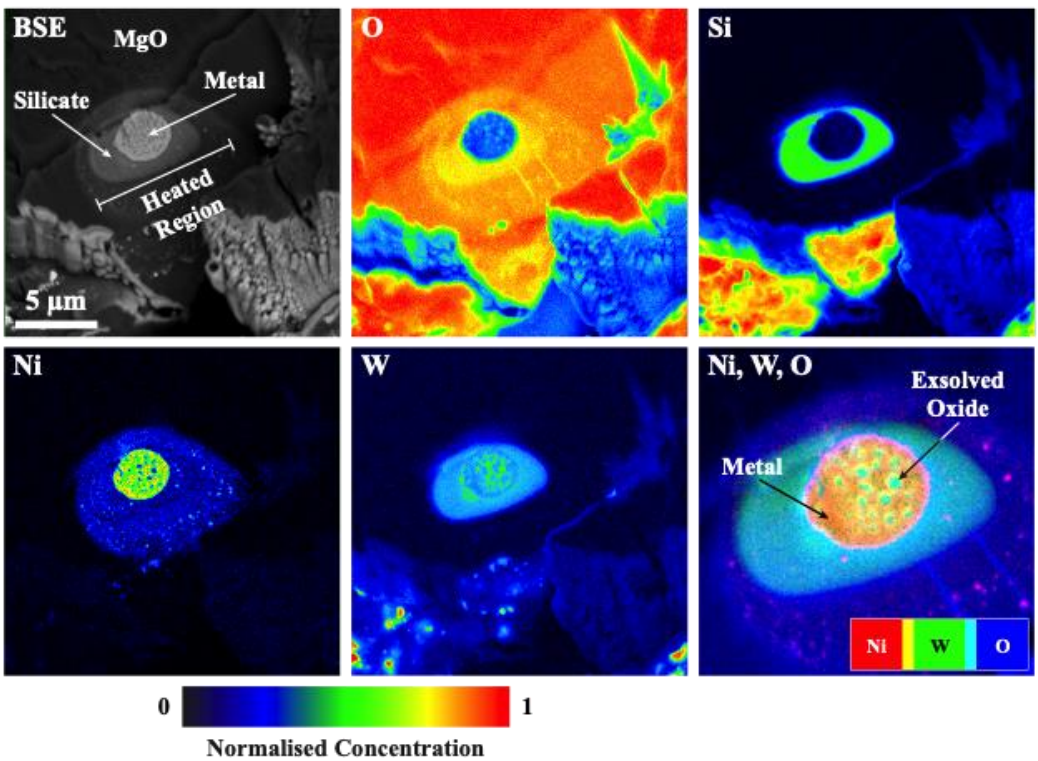

Figure S-5 BSE image and WDS maps for a LH-DAC experiment quenched from ~24 GPa and 3250 K. Within the quenched metal phase at the centre of the heated region, Si, O, and W concentrations are broadly correlated, suggesting they partition preferentially into the oxide phase which is exsolved when the sample is quenched (darker grey blebs in the BSE image). In contrast, Ni remains more concentrated in the metal phase. The final panel combines data for W, Ni, and O, in order to better highlight the concentration of W in the exsolved oxide phase.

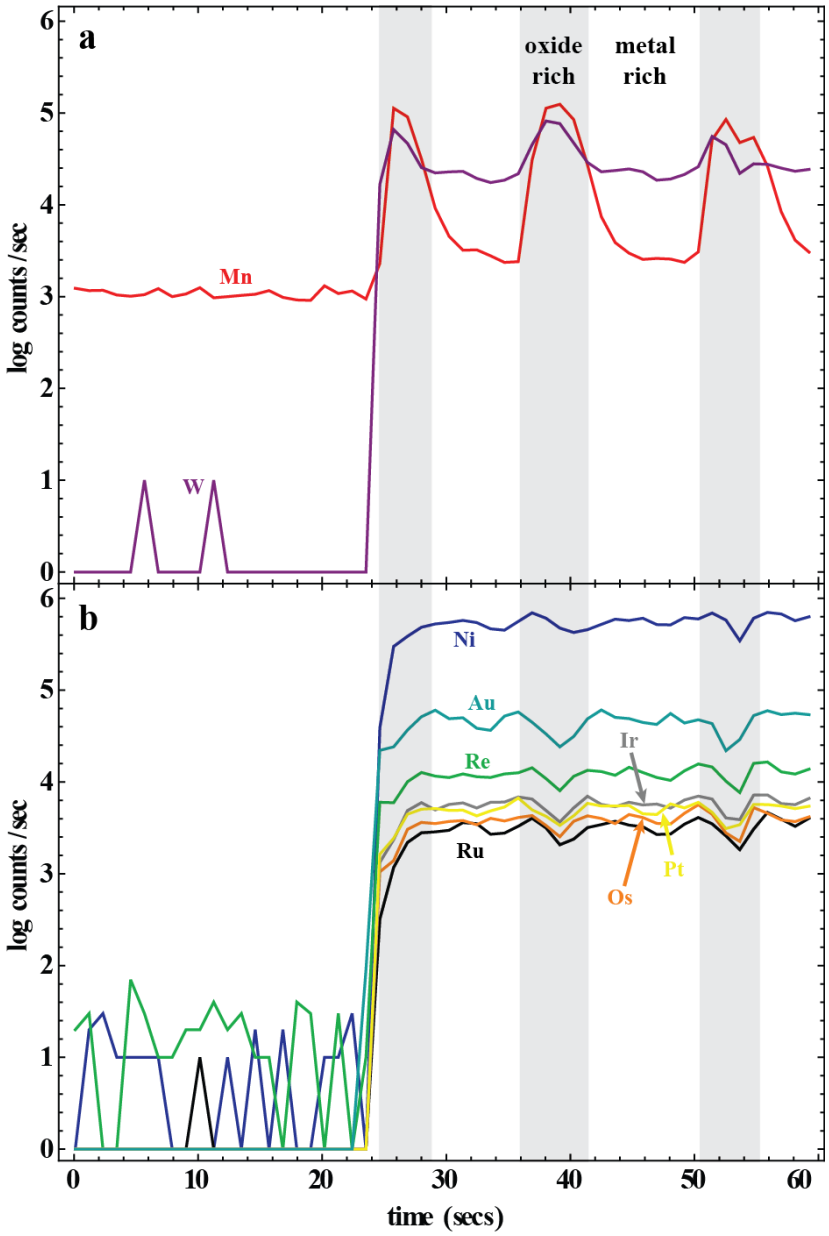

Figure S-6 Time-resolved LA-ICPMS spectra for **(a)** W, Mn and **(b)** the HSEs. Spectra represent a line analysis over a portion of the sample that contained varying amounts of exsolved oxide – leading to heterogeneity in the time-resolved spectrum. Regions of high W and Mn counts/sec represent ablation of an oxide rich part of the sample. Coincident with these high counts/sec regions in the W and Mn spectra are low counts/sec dips in the HSE spectra. This suggests the exsolved oxide phase is enriched in W and Mn, but depleted in the HSEs. The time-resolved spectrum for Ni displays less variation than the other elements, but appears to follow the HSE behaviour. Results from Bennett *et al*. (2014).

Supplementary Information References

Andreasen, R., Sharma, M., Subbarao, K.V., Viladkar, S.G. (2008) Where on Earth is the enriched Hadean reservoir?. *Earth and Planetary Science Letters* 266, 14-28.

Archer, G.J., Mundl, A., Walker, R.J., Worsham, E.A., Bermingham, K.R. (2017) High-precision analysis of $^{182}W/^{184}W$ and $^{183}W/^{184}W$ by negative thermal ionization mass spectrometry: Per-integration oxide corrections using measured $^{18}O/^{16}O$. *International Journal of Mass Spectrometry* 414, 80-86.

Bennett, N.R., Fei, Y. (2014) Element redistribution in Fe-Ni-O alloys by a thermal gradient: implications for siderophile element partitioning and during core-formation and crystallization. *AGU Fall Meeting Abstracts*, DI51A-4344.

Boyet, M., Carlson, R.W. (2006) A new geochemical model for the Earth's mantle inferred from ^{146}Sm–^{142}Nd systematics. *Earth and Planetary Science Letters* 250, 254-268.

Breton, T., Quitté, G. (2014) High-precision measurements of tungsten stable isotopes and application to earth sciences. *Journal of Analytical Atomic Spectrometry* 29, 2284-2293.

Campbell, A.J., Danielson, L., Righter, K., Seagle, C. T., Wang, Y., Prakapenka, V.B. (2009). High pressure effects on the iron–iron oxide and nickel–nickel oxide oxygen fugacity buffers. *Earth and Planetary Science Letters* 286, 556-564.

Caro, G., Bourdon, B., Birck, J.L., Moorbath, S. (2006) High-precision $^{142}Nd/^{144}Nd$ measurements in terrestrial rocks: constraints on the early differentiation of the Earth's mantle. *Geochimica et Cosmochimica Acta* 70, 164-191.

Chabot, N.L., Wollack, E.A., Humayun, M., Shank, E.M. (2015) The effect of oxygen as a light element in metallic liquids on partitioning behavior. *Meteoritics & Planetary Science* 50, 530-546.

Cook, D.L., Schönbächler, M. (2016) High-precision measurement of W isotopes in Fe–Ni alloy and the effects from the nuclear field shift. *Journal of Analytical Atomic Spectrometry* 31, 1400-1405.

de Leeuw, G.A.M., Ellam, R.M., Stuart, F.M., Carlson, R.W. (2017) $^{142}Nd/^{144}Nd$ inferences on the nature and origin of the source of high $^{3}He/^{4}He$ magmas. *Earth and Planetary Science Letters* 472, 62-68.

Doucet, S., Scoates, J.S., Weis, D., Giret, A. (2005) Constraining the components of the Kerguelen mantle plume: A Hf-Pb-Sr-Nd isotopic study of picrites and high-MgO basalts from the Kerguelen Archipelago. *Geochemistry, Geophysics, Geosystems* 6.

Doucet, S., Moreira, M., Weis, D., Scoates, J.S., Giret, A., Allegre, C. (2006) Primitive neon and helium isotopic compositions of high-MgO basalts from the Kerguelen Archipelago, Indian Ocean. *Earth and Planetary Science Letters* 241, 65-79.

Fortenfant, S.S., Rubie, D.C., Reid, J., Dalpé, C., Capmas, F., Gessmann, C.K. (2003) Partitioning of Re and Os between liquid metal and magnesiowustite at high pressure. *Physics of the Earth and Planetary Interiors* 139, 77-91.

Garçon, M., Boyet, M., Carlson, R.W., Horan, M.F., Auclair, D., Mock, T.D. (2018) Factors influencing the precision and accuracy of Nd isotope measurements by thermal ionization mass spectrometry. *Chemical Geology* 476, 493-514.

Gurioli, L., Muro, A., Vlastélic, I., Moune, S., Thivet, S., Valer, M., Villeneuve, N., Boudoire, G., Peltier, A., Bachèlery, P., Ferrazzini, V., Métrich, N., Benbakkar, M., Cluzel, N., Constantin, C., Devidal, J.-L., Fonquernie, C., Hénot, J.-M. (2017) Integrating field, textural, and geochemical monitoring to track eruption triggers and dynamics: a case study from Piton de la Fournaise. *Solid Earth* 9, 431-455.

Horan, M.F., Carlson, R.W., Walker, R.J., Jackson, M., Garçon, M., Norman, M. (2018) Tracking Hadean processes in modern basalts with 142-Neodymium. *Earth and Planetary Science Letters* 484, 184-191.

Huang, S., Humayun, M., Frey, F.A. (2007) Iron/manganese ratio and manganese content in shield lavas from Ko'olau Volcano, Hawai'i. *Geochimica et Cosmochimica Acta* 71, 4557-4569.

Humayun, M., Qin, L., Norman, M.D. (2004) Geochemical evidence for excess iron in the mantle beneath Hawaii. *Science* 306, 91-94.

Ingle, S., Weis, D., Doucet, S., Mattielli, N. (2003). Hf isotope constraints on mantle sources and shallow-level contaminants during Kerguelen hot spot activity since~ 120 Ma. *Geochemistry, Geophysics, Geosystems*, 4(8).

Jackson, M.G., Carlson, R.W. (2012) Homogeneous superchondritic $^{142}Nd/^{144}Nd$ in the mid-ocean ridge basalt and ocean island basalt mantle. *Geochemistry, Geophysics, Geosystems* 13.

Kranendonk, M.J.V., Hickman, A.H., Smithies, R.H., Nelson, D.R., Pike, G. (2002) Geology and tectonic evolution of the archean North Pilbara terrain, Pilbara Craton, Western Australia. *Economic Geology* 97, 695-732.

Kruijer, T.S., Kleine, T. (2018) No ^{182}W excess in the Ontong Java Plateau source. *Chemical Geology* 485, 24-31.

Mundl, A., Touboul, M., Jackson, M.G., Day, J.M., Kurz, M.D., Lekic, V., Helz, R.T., Walker, R.J. (2017) Tungsten-182 heterogeneity in modern ocean island basalts. *Science* 356, 66-69.

Murphy, D.T., Brandon, A.D., Debaille, V., Burgess, R., Ballentine, C. (2010) In search of a hidden long-term isolated sub-chondritic $^{142}Nd/^{144}Nd$ reservoir in the deep mantle: Implications for the Nd isotope systematics of the Earth. *Geochimica et Cosmochimica Acta* 74, 738-750.

Peters, B.J., Carlson, R.W., Day, J.M., Horan, M.F. (2018) Hadean silicate differentiation preserved by anomalous $^{142}Nd/^{144}Nd$ ratios in the Réunion hotspot source. *Nature* 555, 89.

Qin, L., Humayun, M. (2008) The Fe/Mn ratio in MORB and OIB determined by ICP-MS. *Geochimica et Cosmochimica Acta* 72, 1660-1677.

Shofner, G.A. (2011) High Pressure Redox Geochemistry of Tungsten in Metal-Silicate Systems : Implications for Core Formation in the Earth. PhD Thesis, University of Maryland College Park.

Shofner, G.A., Campbell, A.J., Danielson, L.R., Righter, K., Fischer, R.A., Wang, Y., Prakapenka, V. (2016) The W-WO_2 oxygen fugacity buffer at high pressure and temperature: Implications for fO_2 buffering and metal-silicate partitioning. *American Mineralogist* 101, 211-221.

Sobolev, A.V., Hofmann, A.W., Kuzmin, D.V., Yaxley, G.M., Arndt, N.T., Chung, S.L., Danyushevsky, L.V., Elliott, T., Frey, F.A., Garcia, M.O., Gurenko, A.A., Kamenetsky, V.S., Kerr, A.C., Krivolutskaya, N.A., Matvienkov, V.V., Nikogosian, I.K., Rocholl, A., Sigurdsson, I.A., Sushchevskaya, N.M., Teklay, M. (2007) The amount of recycled crust in sources of mantle-derived melts. *Science* 316, 412-417.

Thibault, Y., Walter, M. J. (1995) The influence of pressure and temperature on the metal-silicate partition coefficients of nickel and cobalt in a model C1 chondrite and implications for metal segregation in a deep magma ocean. *Geochimica et Cosmochimica Acta*, 59, 991-1002.

Trieloff, M., Kunz, J. (2005) Isotope systematics of noble gases in the Earth's mantle: possible sources of primordial isotopes and implications for mantle structure. *Physics of the Earth and Planetary Interiors* 148, 13-38.

Vlastélic, I., Lewin, E., Staudacher, T. (2006) Th/U and other geochemical evidence for the Reunion plume sampling a less differentiated mantle domain. *Earth and Planetary Science Letters* 248, 379-393.

Vlastélic, I., Deniel, C., Bosq, C., Télouk, P., Boivin, P., Bachèlery, P., Famin, V., Staudacher, T. (2009) Pb isotope geochemistry of Piton de la Fournaise historical lavas. *Journal of Volcanology and Geothermal Research* 184, 63-78.

Vlastélic, I., Menard, G., Gannoun, A., Piro, J.L., Staudacher, T., Famin, V. (2013) Magma degassing during the April 2007 collapse of Piton de la Fournaise: the record of

semi-volatile trace elements (Li, B, Cu, In, Sn, Cd, Re, Tl, Bi). *Journal of Volcanology and Geothermal Research* 254, 94-107.

Vlastélic, I., Di Muro, A., Bachèlery, P., Gurioli, L., Auclair, D., Gannoun, A. (2018) Control of source fertility on the eruptive activity of Piton de la Fournaise volcano, La Réunion. *Scientific reports* 8, 14478.

Völkening, J., Köppe, M., Heumann, K.G. (1991) Tungsten isotope ratio determinations by negative thermal ionization mass spectrometry. *International Journal of Mass Spectrometry and Ion Processes* 107, 361-368.

Wiemer, D., Schrank, C.E., Murphy, D.T., Hickman, A.H. (2016) Lithostratigraphy and structure of the early Archaean Doolena Gap greenstone belt, East Pilbara Terrane, Western Australia. *Precambrian Research* 282, 121-138.

Woodhead, J. (2002) A simple method for obtaining highly accurate Pb isotope data by MC-ICP-MS. *Journal of Analytical Atomic Spectrometry* 17, 1381-1385.